Quasi-Distributed Torque and Displacement Sensing on a Series Elastic Actuator's Spring Using FBG Arrays Inscribed in CYTOP Fibers

Arnaldo G. Leal-Junior, *Member, IEEE*, Antreas Theodosiou, *Student Member, IEEE*, Rui Min, Jonathan Casas, Camilo R. Díaz, *Student Member, IEEE*, Wilian M. dos Santos, Maria José Pontes, *Member, IEEE*, Adriano A. G. Siqueira, *Member, IEEE*, Carlos Marques, Kyriacos Kalli, *Member, IEEE*, and Anselmo Frizera, *Member, IEEE*

***Abstract*— We report the application of fiber Bragg grating (FBG) arrays in polymer optical fibers for the quasi-distributed displacement and torque sensing in a series elastic actuator's spring. The arrays were inscribed in cyclic transparent optical polymer fiber through the direct-write, plane-by-plane inscription method using a femtosecond laser. Two arrays with four FBGs each were positioned on a rotary spring, and a numerical analysis using the finite-element method was performed to evaluate the sensors' behavior under different loading conditions. Experimental tests were performed on the spring, and the results show that the FBGs responses follow the predicted numerical simulations. In addition, a Kalman filter was applied on the response of the FBGs for sensor fusion, leading to a more accurate torque estimation, where the relative error for the torque estimation was improved by a factor of 7. Furthermore, transverse forces were applied on the predefined points of the spring in order to show the ability of the quasi-distributed sensor approach to identify external mechanical disturbances on the spring.**

***Index Terms*— Polymer optical fiber, fiber Bragg gratings, series elastic actuators, torque sensor, Kalman filter.**

Manuscript received January 9, 2019; revised February 7, 2019; accepted February 7, 2019. Date of publication February 12, 2019; date of current version May 6, 2019. This work was supported in part by Coordenação de Aperfeiçoamento de Pessoal de Nível Superior, financing code 001, under Grant 88887.095626/2015-01, in part by Fundação de Amparo à Pesquisa e Inovação do Espírito Santo under Grant 72982608 and Grant 84336650, in part by National Council for Scientific and Technological Development under Grant 304192/2016-3 and Grant 310310/2015-6, and in part by the National Funds (OE) through the Fundação para a Ciência e a Tecnologia (FCT), I.P., in the scope of the framework contract foreseen in the numbers 4, 5, and 6 of the article 23, of the Decree-Law 57/2016, of August 29, changed by Law 57/2017, of July 19. The work of C. Marques was supported in part by the National Funds through the FCT/Ministério da Educação e Ciência under Grant UID/EEA/50008/2019 and in part by the European Regional Development Fund under the PT2020 Partnership Agreement. The associate editor coordinating the review of this paper and approving it for publication was Dr. Daniele Tosi. *(Corresponding author: Arnaldo G. Leal-Junior.)*

A. G. Leal-Junior, C. R. Díaz, M. J. Pontes, and A. Frizera are with the Graduate Program of Electrical Engineering, Federal University of Espírito Santo, Vitória 29075-910, Brazil (e-mail: leal-junior.arnaldo@ieee.org; c.rodriguez.2016@ieee.org; mjpontes@ele.ufes.br; frizera@ieee.org).

A. Theodosiou and K. Kalli are with the Photonics and Optical Sensors Research Laboratory, Cyprus University of Technology, 3036 Limassol, Cyprus (e-mail: theodosiou.antreas@gmail.com; kkalli@cytanet.com.cy).

R. Min is with the ITEAM Research Institute, Universitat Politècnica de València, 46022 Valencia, Spain (e-mail: rumi@doctor.upv.es).

J. Casas is with the Escuela Colombiana de Ingeniería Julio Garavito, Bogotá 111166, Colombia (e-mail: jonathan.casas@escuelaing.edu.co).

W. M. dos Santos and A. A. G. Siqueira are with the Department of Mechanical Engineering, Engineering School of São Carlos, University of São Paulo, São Paulo 13566-590, Brazil (e-mail: wilianmds@sc.usp.br; siqueira@sc.usp.br).

C. Marques is with the Instituto de Telecomunicações, University of Aveiro, Aveiro 3810-193, Portugal, and also with the Physics Department, I3N, University of Aveiro, Aveiro 3810-193, Portugal (e-mail: carlos.marques@ua.pt).

Digital Object Identifier 10.1109/JSEN.2019.2898722

I. Introduction

STIFFNESS reduction is a current trend for the design of robots and actuators [1]. The so-called soft robotics (where flexible structures and actuators are used) may be regarded as one of the leading technologies for the development of next generation robots [2]. Therefore, stiffness reduction is especially important in biomedical applications, in which the robotic device has to comply with biocompatibility and biomimicry requirements [3]. Series elastic actuators (SEAs) are one of the first technologies to break the "stiffer is better" paradigm that endured for many decades in robots design [4]. Since their first report in 1995, SEAs have been used on the design of robots [5], prostheses [6], orthosis [7] and exoskeletons [8]. Even now, more than 20 years later, SEAs are regarded as a core technology on actuator's design of flexible/compliant robots [9].

A SEA is comprised of an elastic element between the motor unit and the load, which (for wearable robots for gait rehabilitation and assistance purposes) leads to an increase of the compliance between the wearable robot and the user [7]. This feature leads to an actuator with low output impedance, reducing the risk of accidents with the user. In addition, the bandwidth reduction caused by the spring is not an issue in wearable applications, as human movement also occurs in low frequencies [10]. Thus, SEAs are successfully employed in wearable robots for gait rehabilitation with advantages over conventional therapies related to their higher repeatability, the quantitative feedback of the patient recovery and possibility of treatment customization [11].

Hooke's law states that, if the spring operates within its linear region, the force (or torque) is proportional to the displacement, where this proportionality is given by the spring stiffness. Hence, it is possible to estimate the force (or torque) in the actuator by means of only measuring the spring displacement, which simplifies the actuator instrumentation [4]

for robust force control and impedance controllers [7], [9]. For this reason, encoders and potentiometers are conventionally applied in the SEAs instrumentation [12]. However, other than their sensitivity to electromagnetic fields, these sensors need to be precisely assembly in the spring axle, which results in a less compact system [13]. Since the sensors are not directly positioned on the spring, the measurement is also sensitive to backlash on the motor unit, which generally needs compensation, as reported in [7].

Polymer optical fibers (POFs) have seen significant recent evolution, from restricted applications in short communication systems to highly sensitive and reliable sensor and communication systems [14], [15]. Such widespread use of POF sensors is mainly due to their advantages over the silica counterparts related to their material features, which include lower Young's modulus, higher strain limits, higher fracture toughness and impact resistance [14]. Furthermore, POFs share the advantages of silica optical fibers for sensors applications, which include lightweight, compactness, multiplexing capabilities and electromagnetic field immunity [14]. For these reasons, POF sensors were already proposed in the literature to measure parameters such as temperature [16], strain [17], angle [18], humidity [19], pressure [20], force [21] and acceleration (even in ultrasound region) [22], where these parameters are also important in a robot instrumentation.

Applications of POF sensors in robot instrumentation and in movement analysis have already been proposed [23]. In previous work, the feasibility of rotary SEA instrumentation with POF sensors was demonstrated [13], where it is possible to measure the spring deflection directly on the spring, instead of placing a sensor on the output axis (as it is made with encoders and potentiometers). Among the different technologies of optical fiber sensing, fiber Bragg gratings (FBGs) offer good multiplexing capabilities, which enable the inscription of long sensor arrays in the same fiber [24]. FBGs have been inscribed in POFs since 1999 [25] with increasing degree of success and greater efforts have been made to realize polymer optical fiber Bragg gratings (POFBGs) inscription in commercially available fibers [26], [27], which is challenging due to their larger core diameters and therefore multimode operation, resulting in multi-peak spectra [28]. In order to overcome this issue, Theodosiou *et al.* [29] showed a single peak spectrum obtained in a multimode POF through the optimization of the inscription parameters to control the coupling between the grating and the core modes using a suitable femtosecond (fs) laser inscription (direct-write, plane-by-plane inscription method [30]). Cyclic transparent optical polymer (CYTOP) POFs were employed due to their lower optical losses, and it was possible to inscribe long sensor arrays operating in the 1550 nm wavelength region [27], [31]. Actually, it is an important breakthrough, since it leads to realistic application of POF-based sensors with commercially available FBG interrogators that generally operates at 1550 nm wavelength region.

The feasibility of applying FBG sensors on strain sensing in a rotary spring was presented in [32]. However, the employed FBGs were inscribed in silica fibers, this inhibits their applications in regions that have higher strain in the spring, and only two FBGs were placed on this elastic element. If a higher number of FBG sensors are placed on the rotary spring it would be possible to reconstruct the spring shape when a loading is applied through the analysis of the wavelength shift of each FBG. It is also possible to infer and reject mechanical disturbances on the spring when additional FBG sensors are used. The application of FBGs in shape reconstruction of structures was demonstrated in [33]. This feature is especially desirable when the SEA suffers from mechanical perturbations. Even though the elastic element acts as a mechanical low-pass filter, the actuator may be subjected to transversal loading with lower frequency, especially in wearable applications due to inherent three dimensional behavior of human movement [34]. These mechanical disturbances can lead to measurement errors in conventional potentiometers and encoders due to their sensitivity to misalignments.

Considering the advantages of POF sensors in conjunction with the possibility of inscribing long arrays in commercially available low-loss POFs, this paper presents the instrumentation of the series elastic actuator's spring designed in [7] with two FBG arrays in CYTOP fibers, were each sensor array has 4 FBGs. Thus, 8 FBGs are distributed on the spring, enabling a multi-point strain measurement on the spring. This configuration results in three advantageous features that will be further explored: (i) shape reconstruction of the spring under deformation, (ii) improved accuracy of the torque measurements using Kalman filtering and (iii) identification and rejection of mechanical disturbances caused by arbitrary external loading. The sensor operation and the spring deflection under different loadings are estimated through a numerical analysis using the finite element method (FEM) and confirmed through experimental analysis. Comparing to our previous work [32], in this work, we use POFs that enable higher dynamic range and sensitivity than their silica counterparts. In addition, the used array with 7 FBGs enables a reliable estimation of the torque through sensor fusion algorithms as well as mechanical disturbance rejection in the actuator. Thus, the proposed work shows a novel approach for SEA's instrumentation.

II. POFBG-Arrays Positioning and Experimental Setup

The FBGs were positioned on the spring as shown in Fig. 1(a), where a lever was positioned in the spring output shaft for the application of predefined displacements and torques. The fiber was fixed on the spring by means of 3D-printed supports placed between the FBGs and thermoplastic glue. The spring was fixed in a base, positioned on a fixed support to limit flexion and extension movements to only one plane. Figure 1(b) shows a back view of the spring, where it can be seen the encoder E5 series (US digital, USA) positioned on the output shaft (used for comparison with the FBG sensors). The spring showed linear behavior for torque less than 30 Nm, with a stiffness constant of 92 Nm/rad for flexion and 96 Nm/rad for extension, as characterized in [7], which enabled torque estimation through the spring angular deflection.

Regarding the POFBG arrays' inscription, a commercial multimode CYTOP fiber (Chromis Fiberoptics Inc.) with

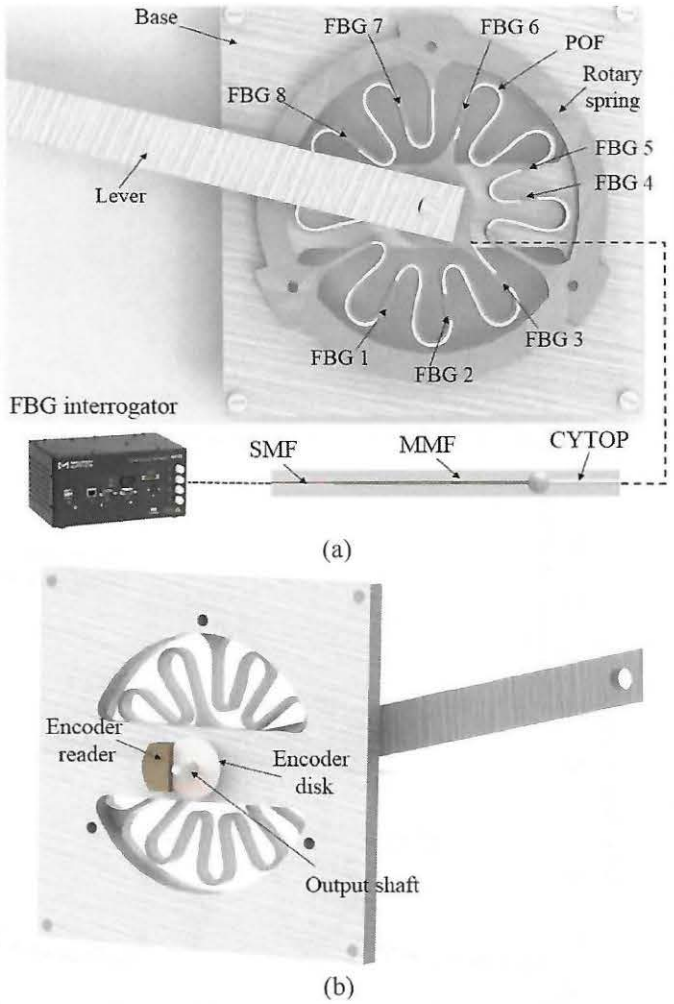

Fig. 1. (a) Front view of the spring with the FBG sensor positions, schematic representation of the POF connectorization and FBG interrogator. (b) Rear view of the spring with the encoder used for comparison purposes.

graded index was used. The dimensional characteristics of this fiber are: 120 μm core diameter, 20 μm cladding thickness and a polycarbonate overcladding that result in a total fiber diameter of 490 μm. The inscription was performed with an fs laser system (HighQ laser femtoREGEN) centered at 517 nm with a 220-fs pulse duration using the direct-write, plane-by-plane inscription method [27], [29]. In this case, the POF is positioned on an air-bearing translation stage (with nanometer resolution) for its motion during inscription. The beam is focused on the POF with a $\times$50 objective lens and it is accurately controlled to guarantee that the refractive index modifications are induced at the center of fiber core, where a pulse energy of ~80 nJ and the repetition rate of 5 kHz were used. The FBG arrays are at 1550 nm wavelength region and each FBG has a physical length of 1.4 mm. Thereafter, an annealing is performed on the arrays (as described in [35]) and the FBG array is butt-coupled to a multimode silica fiber using a UV-curing glue (Loctite AA 3936, USA), which is fusion spliced to a single mode silica pigtail in order to obtain a smooth variation of the core diameter (see Fig. 1(a)).

Firstly, numerical analysis is undertaken on the spring to evaluate its deflection with torque and the strain distribution when a transverse force is applied on arbitrary points of the spring. Then, experimental evaluation is performed in which three different flexion and extension displacements are applied on the spring using the lever connected to the spring shaft (see Fig. 1). In addition, transverse forces are applied to the spring to evaluate the FBG sensors in identifying these forces and whether flexion and extension displacements are possible. In order to obtain a reliable measurement of the flexion and extension on the spring, a Kalman filtering [36] is applied on the response of the FBG array using the known displacements applied to the spring as a reference for the filter estimation.

The Kalman filter is a recursive filter that estimates the state of a system from a series of measurements. In this way, the measurements of each sensor and the reference are used to generate an estimate of the system measurements as a whole. This estimate has a lower error than the measurement of each sensor analyzed separately [37]. The filter uses a procedure that utilizes a definition of weights for the sensors. The sensors that display lower errors have higher weight in the estimation of the state, in comparison with sensors that display greater uncertainty. Defined weights are, in fact, the covariance of each sensor. The lower the covariance the higher the weight of the result obtained by the sensor in the final estimation [38]. The Kalman filter is employed in sensor fusion due its simplicity and ease of implementation and optimization [38]. Interested readers may refer to [39] for the detailed description, modeling and applications of the Kalman filter. If the system is in state space, the prediction is made through (1) and (2); and updated through (3), (4) and (5).

$$\hat{x}_{k|k-1} = A\hat{x}_{k-1|k-1}, \tag{1}$$

$$P_{k|k-1} = A P_{k-1|k-1} A', \tag{2}$$

$$G = P_{k|k-1} C' (C P_{k|k-1} C' + R), \tag{3}$$

$$P_{k|k} = (I - GC) P_{k|k-1}, \tag{4}$$

$$\hat{x}_{k|k} = \hat{x}_{k|k-1} + G(z_k - C\hat{x}_{k|k-1}), \tag{5}$$

where A and C are the transition matrices of state (at time k) and observability, respectively, which have unitary values in this case, since, presumably, the sensor does not alter the system dynamics. G is the Kalman gain, P is the covariance matrix, z_k is the measured signal, R is the sensors covariance, I is the identity matrix and $\hat{x}_{k\backslash k}$ is the estimated state at time k given observations up to and including at time k. Thus, the response of each FBG results in the z_k matrix used on the state prediction in conjunction with the transition matrix A (unitary) and the sensor covariance matrix P. Then, the prediction is updated by means of estimating the Kalman gain (G) from (3) in which the covariance (R) of each sensor obtained in the calibration procedure is used to provide such estimation. Thereafter, the covariance matrix and the estimated state are updated, resulting in a more accurate estimation of the torque, in this case.

III. Numerical Analysis

In order to evaluate the spring deflection at each of the FBG sensor locations, a numerical simulation is performed on the spring through FEM analysis using Ansys Workbench 15.0. In the analysis, the outer cylinder is fixed, whereas torque is applied to the inner cylinder (where the output shaft is located).

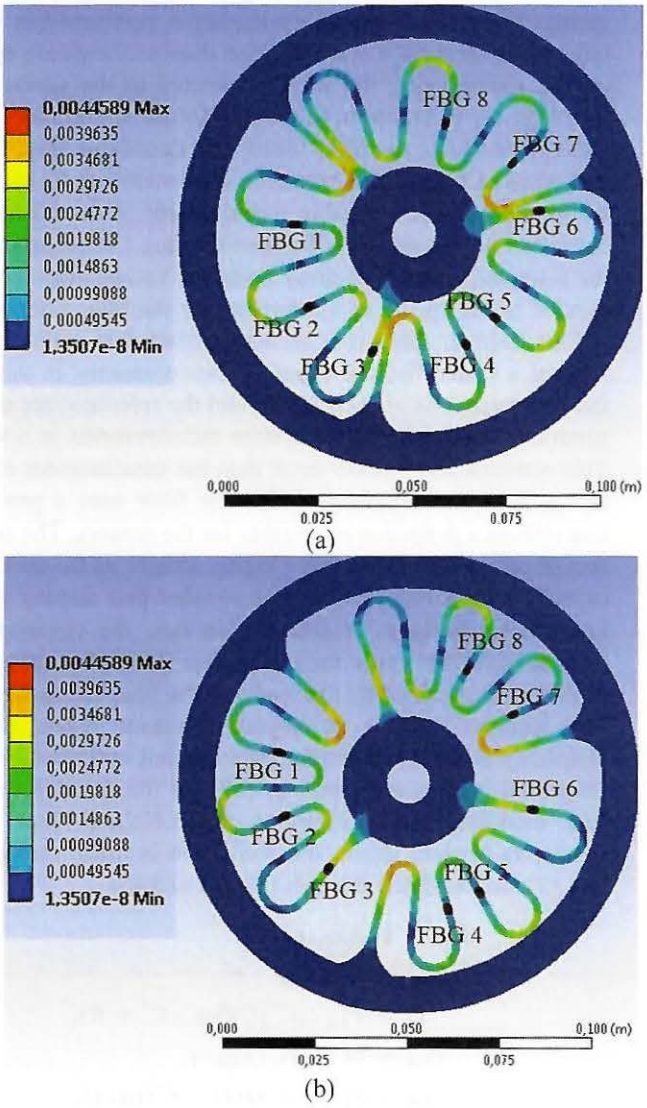

Fig. 2. Equivalent Von Mises strain (m/m) on the spring under (a) flexion and (b) extension.

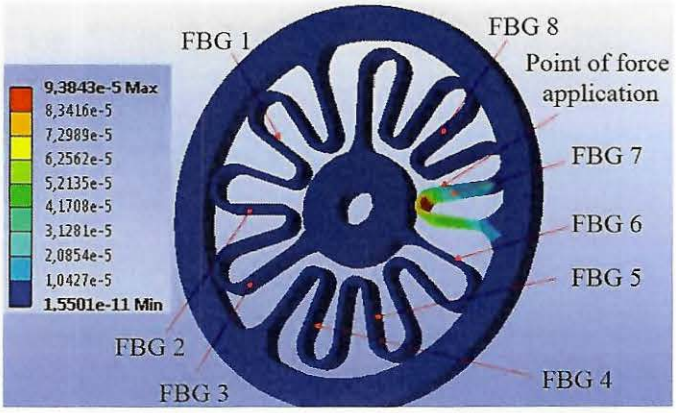

Fig. 3. Equivalent strain (m/m) on the spring under a transverse force of 5 N.

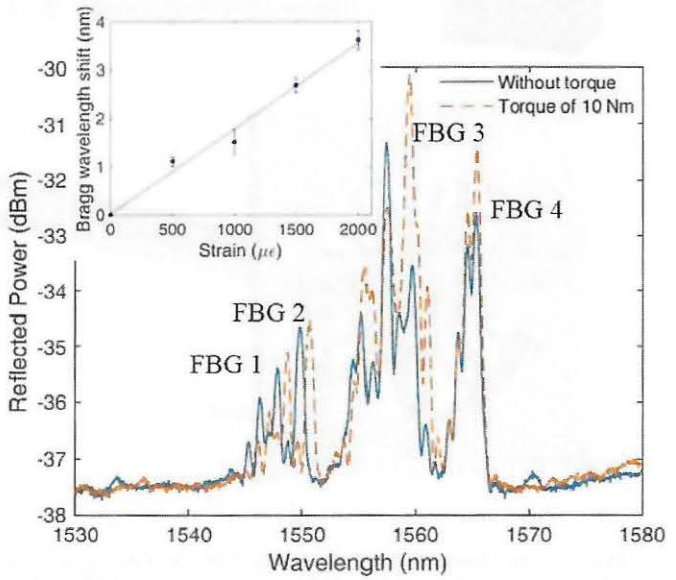

Fig. 4. FBG array spectra with and without torque. The inset show the mean and standard deviation of the strain response of the FBG arrays.

Figure 2 shows the results obtained in the simulation for flexion (Fig. 2(a)) and extension (Fig. 2(b)), where torque of the same magnitude (20 Nm), but different direction (flexion and extension), was applied.

The simulation results shown in Figure 2 indicate that there is a strain variation at all points analyzed proportional to the applied torque (following Hooke's law). It also shows the polarity of the strain, where the equivalent Von Mises strain values are similar on flexion and extension cases, but with different directions for the deformation. If the clockwise direction (extension cycle) is considered the positive direction, the strain components at the counter-clockwise direction have the same magnitude, but with the negative signal (indicating the different direction). After verifying the spring behavior under flexion/extension cycles, another numerical analysis is made to verify the effect of an external force applied on the front plane of the spring (see Fig. 3). This transverse force acts as a mechanical disturbance on the system, which needs to be evaluated by the sensor array. Figure 3 shows the strain on the spring after the application of an arbitrary transverse force, which has 5 N magnitude in the simulation.

The transverse force simulation shows that there is a stress concentration on regions close to the point of force application, which leads to higher strain in the FBGs close to this region. Thus, by analyzing the response of all the FBGs on the spring, it is possible to infer if the strain is caused by a transverse force or by the flexion/extension, since the position of each FBG is known. Therefore, a simple and straightforward analysis of whether the spring deflection is due to flexion and extension or transverse mechanical disturbances is extracted from the wavelength shifts of FBGs positioned on the spring. These results are subsequently compared with the case where only flexion and extension torques are applied to the spring.

IV. Experimental Analysis

The arrays in the CYTOP fiber were inscribed with the direct-write, plane-by-plane method using the fs laser as discussed in Section II. The spectra of an array with 4 FBGs is presented in Fig. 4 under different torques, where it

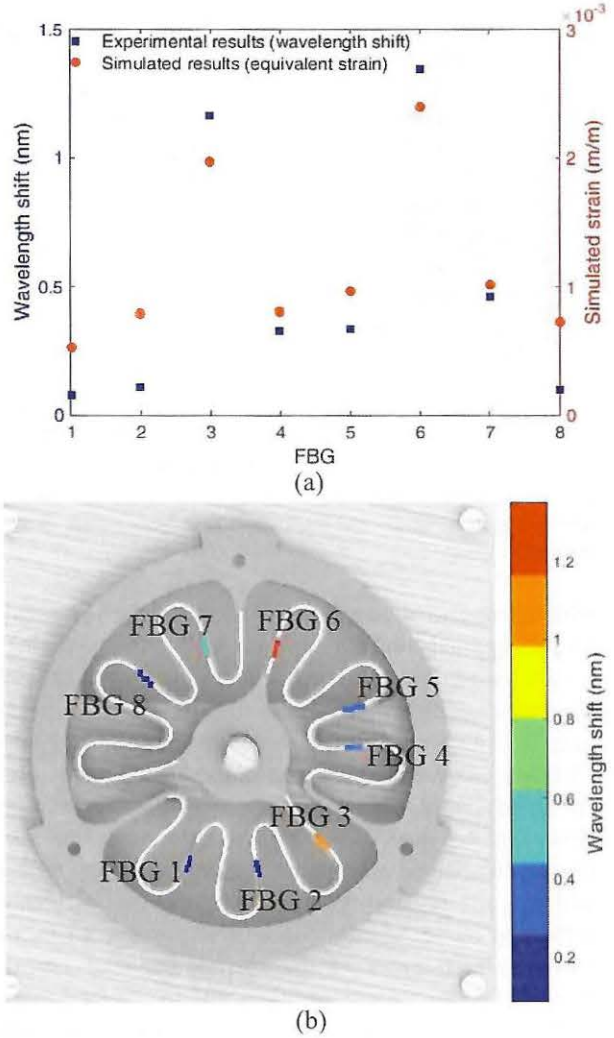

Fig. 5. (a) Wavelength shift for the 8 FBGs and simulated strain on the region of each FBG. (b) Wavelength shift at each region of the spring as a tool for shape reconstruction of the device under deformation.

can be seen the wavelength shift on the FBGs. The reason to present those 4 FBGs is to improve the visualization of the torque influence on the FBGs spectra. In addition, the inset of Fig. 4 shows the mean and standard deviation of the 8 FBGs responses under different strains. The sensors sensitivities are 1.8 ± 0.2 pm/$\mu\varepsilon$, where such sensitivities are related to the annealing treatment performed on the fiber as discussed in [35].

As shown in Section III, the deformation at each region of the spring is different. Thus, each FBG will be subjected to different strains. In order to compare the simulated and experimental results, a constant displacement of 0.2 rad is applied on the spring in the clockwise direction (extension), which results in a torque of ~18.4 Nm, considering the spring stiffness of 92 Nm/rad [7]. Figure 5 shows the obtained wavelength shift for each FBG at a constant torque, where the experimental results obtained from the FBGs wavelength shift are compared with the strain obtained in the simulations in the region of each FBG (see Fig. 2(a)). Since the increase of the strain leads to an increase of the

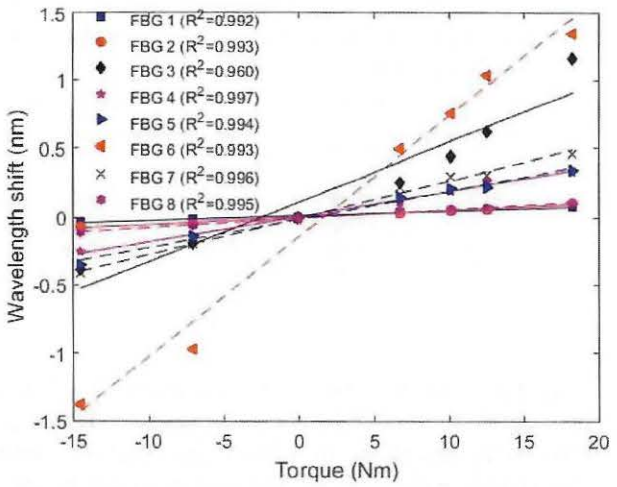

Fig. 6. FBGs responses as a function of the applied torque on the spring.

FBGs wavelength shift, the results of Fig. 5(a) shows that the FBGs present similar behavior when compared to the one predicted by the numerical analysis. It is noteworthy that the comparison between the sensors responses and the simulated strain is performed only to check whether or not the FBGs follow the same pattern of the strain at each region, since, as verified in [7], there are differences between the simulated and measured strains on the spring due to material anisotropy and numerical errors. Thus, the qualitative analysis shown in Fig. 5(a) indicates the possibility of using the response of each FBG for the shape reconstruction of the spring under flexion and extension as shown in Fig. 5(b), where a colormap with the wavelength shift of each respective FBG is placed on the spring at the region where the wavelength shift was measured.

The behavior of each FBG inscribed in POF is evaluated under different flexion and extension torques, where extension torques are negative and the flexion ones have the positive signal. Figure 6 shows the response of the 8 FBGs, individually. As shown in simulated and experimental results in Fig. 5(a) and confirmed in Fig. 6, FBGs 3 and 6 show the largest variation whereas FBGs 1, 2 and 8 presented the lowest wavelength shift, which is strictly related to their positioning on the rotary spring.

In addition, Fig. 6 shows a linear relation between each FBG and the applied torque, where each FBG has its own linear regression equation depending on its position on the rotary spring. The linear regression terms (a and b) of FBGs 1 to 8 as a function of the torque is presented in Table I, where a is the sensitivity (in nm/Nm) and b is the offset (in nm) in the linear regression. It is worth noting that each equation has the type shown in (6), where T is the torque applied on the spring and $\Delta\lambda$ is the wavelength shift. Furthermore, by isolating the T term in (6), it is possible to obtain the torque estimated by each FBG sensor. In this way, the estimated responses of the FBGs are compared with the applied torque and the root mean squared error (RMSE) between the estimated and applied torques are also shown in Table I for each FBG, where 3 measurements were made. Comparing with the

TABLE I
LINEAR REGRESSION AND TORQUE RESPONSE OF EACH FBG

FBG	*a (nm/Nm)*	*b (nm)*	RMSE (Nm)
1	3.4×10^{-3}	1.1×10^{-2}	1.37
2	5.0×10^{-3}	-1.6×10^{-3}	1.24
3	4.3×10^{-2}	1.1×10^{-1}	3.14
4	1.8×10^{-2}	4.0×10^{-3}	0.87
5	2.1×10^{-2}	-1.7×10^{-2}	1.16
6	8.8×10^{-2}	-1.5×10^{-1}	1.29
7	2.7×10^{-2}	-6.0×10^{-3}	0.89
8	6.5×10^{-3}	-9.3×10^{-3}	1.10

silica FBGs on the same spring (presented in [32]), sensitivities up to 8 times higher were obtained with the proposed FBG array inscribed in POFs. This higher sensitivity in conjunction with ease of installation highlight the advantages of using POFs instead of silica fibers in this particular application.

$$\Delta\lambda = aT + b. \tag{6}$$

The RMSEs shown in Table I are related to nonlinearities on the linear regression of each FBG, whereas the differences on the coefficients a and b indicate the influence of the FBGs positioning on their responses. It is worth noting that such feature was already anticipated on the numerical analysis performed. As depicted in Fig. 6, FBG 3 shows the lowest determination coefficient (R^2) with the linear regression due to nonlinearities on the sensor behavior, which also resulted in asymmetry on the response comparing the flexion and extension cycles that can be related to the fiber positioning on this specific region on the spring. Thus, FBG 3 also showed the highest RMSE in comparison to the estimated applied torque. For the other FBGs, the RMSE was ~1.0 Nm and the R^2 of these sensors exceeded 0.99 (see Fig. 6), which can be regarded as low errors if the whole tested torque range is considered. Considering all 8 FBGs, the mean RMSE is 1.39 ± 0.73 Nm, which represents a relative error of about 4.2% when the whole torque range (about 32 Nm) is evaluated. However, there are 8 sensors providing the same information, i.e., flexion/extension torque on the rotary spring. For this reason, it is possible to apply sensor fusion algorithms in the sensors responses in order to obtain a more accurate measurement. Therefore, the Kalman filter (described in Section II) is applied on the sensors responses. The parameters of the filter are estimated recursively by comparing the sensor response after the sensor fusion with the reference torque in order to obtain the lowest possible error for the sensors. In this case, the covariance of each sensor (R_{1-8}) is obtained based on the error of each sensor, where the lower errors resulted in lower covariance values as depicted in Fig. 7. The FBGs torque estimation after the sensor fusion is shown in Fig. 7, where the applied torque is compared with the estimated one (with the fusion of the 8 FBG sensors).

Regarding the results of Fig. 7, there is a substantial decrease on the sensor RMSE when compared to the applied torque, which is also related to the increase of the sensor linearity ($R^2 = 0.999$). Comparing to the results shown in Table I, there is a seven-fold decrease of the sensor's RMSE,

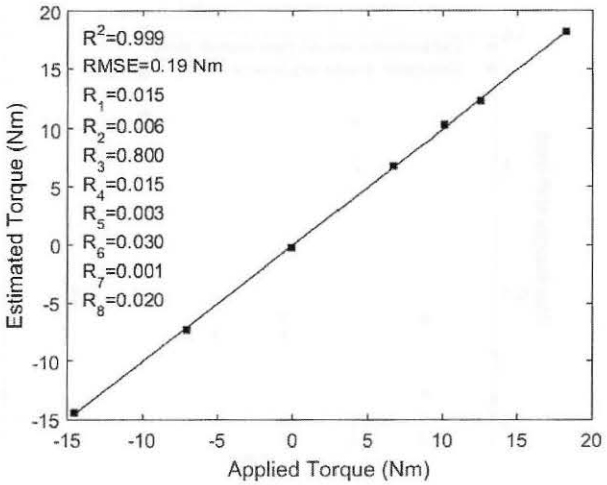

Fig. 7. Torque estimated after the sensor fusion between 8 FBGs compared with the applied torque. The RMSE and covariance matrix values are also presented.

which leads to a much more accurate measurement of the torque applied on the spring. In addition, if the whole torque range is considered, the sensor's response following the application of the Kalman filter results in a deviation of only 0.59%. These results show the feasibility of applying a FBG array in conjunction with sensor fusion techniques on the spring to obtain highly accurate and reliable sensor systems. However, the quasi-distributed measurements on the spring brings another advantageous feature for the sensor system, which is the possibility of rejecting external mechanical disturbances on the spring. Since it is possible to estimate the strain at each point of the spring, one can estimate if a given deflection on the spring is due to the flexion/extension torques or due to transverse forces on the spring, which are regarded as mechanical disturbances. In order to verify this assumption, arbitrary loads are applied in 5 points of the spring as shown in Fig. 8(a) and the wavelength shift of each FBG is presented in the tool for spring shape reconstruction for 2 cases. Moreover, all the transverse force conditions and flexion/extension torques are shown in Fig. 8(b), where the subplot of the top shows the FBG responses at 3 different flexion/extension torques, whereas the one at the bottom of Fig. 8(b) shows the FBG responses at the 5 transverse force conditions.

In Fig. 8, all 5 cases analyzed have shown an increase of the wavelength shift on the FBGs close to the point of transverse force application. As expected, the shift was higher on FBGs 3 and 6, since these sensors are positioned on the region of the highest strain on the spring, as predicted by the numerical simulation and confirmed in the experimental analysis. As shown in Figs. 5 and 6, the response of each FBG is linear, which means that the response of the sensors follow a well-defined pattern when only flexion and extension are applied on the spring. Hence, a simple and straightforward manner to identify external disturbances on the spring is by comparing the strain distribution (from the wavelength shift of all FBGs) on the spring for a given loading condition with a reference strain condition. The reference condition is obtained when only flexion and extension are applied on the spring.

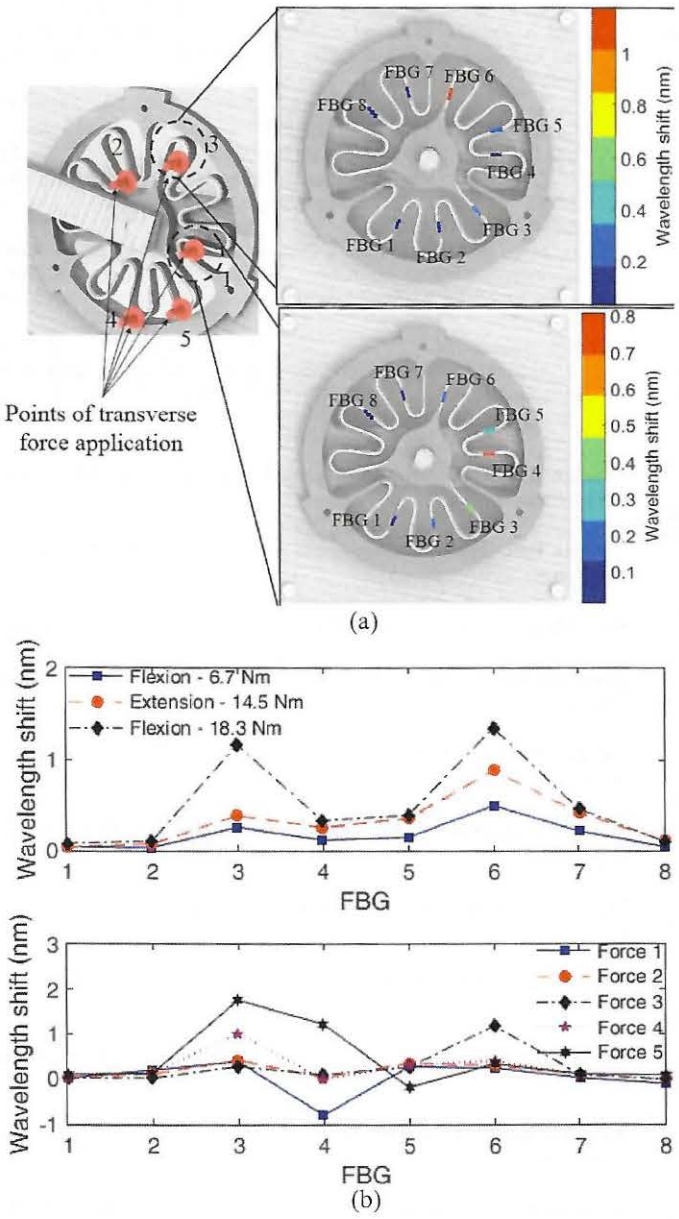

Fig. 8. (a) Force application points and wavelength shift at each region of the spring at 2 transverse force cases. (b) Wavelength shift of each FBG at flexion/extension torques (top) and transverse force conditions (bottom).

V. Conclusions

This paper has presented the instrumentation of a SEA's spring with FBG arrays inscribed in CYTOP fibers. Two arrays (each one with 4 FBGs) were inscribed in the POF using the direct write, plane-by-plane inscription with the fs laser. The 8 FBGs were positioned on the rotary spring and a numerical simulation using FEM was performed in order to predict the sensor's behavior under flexion and extension torques as well as transverse forces. An experimental analysis was made on the spring for the both conditions (flexion/extension torques and transverse forces). The experimental results confirmed the initial assumptions that the proposed quasi-distributed measurement on the spring offers advantageous features to the SEA's instrumentation. These advantages are the possibility of displacement measurement in different points of the spring, which can aid on the design and optimization of the spring for a given operation condition or design requirement. Moreover, there is the possibility of obtaining more information of a single variable by means of the application of the Kalman filter for sensor fusion, resulting in a seven-fold decrease of the torque estimation error when compared with the results without the sensor fusion. The quasi-distributed sensor system on the spring also enabled the identification of external mechanical disturbances on the spring, which can aid on the robotic device control. In summary, this paper shows not only the feasibility, but also the advantages of applying a FBG array on the instrumentation of an elastic element, which is well aligned with the instrumentation requirements of soft robots and compliant structures. Thus, the proposed methodology can be applied in different springs and in different flexible structures of soft robotics, which will be explored in future work.

References

[1] J. Z. Gul *et al.*, "3D printing for soft robotics—A review," *Sci. Technol. Adv. Mater.*, vol. 19, no. 1, pp. 243–262, Dec. 2018.
[2] M. Manti, V. Cacucciolo, and M. Cianchetti, "Stiffening in soft robotics: A review of the state of the art," *IEEE Robot. Automat. Mag.*, vol. 23, no. 3, pp. 93–106, Sep. 2016.
[3] M. Cianchetti, C. Laschi, A. Menciassi, and P. Dario, "Biomedical applications of soft robotics," *Nature Rev. Mater.*, vol. 3, pp. 143–153, May 2018.
[4] G. A. Pratt and M. M. Williamson, "Series elastic actuators," in *Proc. IEEE/RSJ Int. Conf. Intell. Robots Syst. Hum. Robot Interact. Cooperative Robots*, vol. 1, Aug. 1995, pp. 399–406.
[5] K. Abe, T. Suga, and Y. Fujimoto, "Control of a biped robot driven by elastomer-based series elastic actuator," in *Proc. IEEE Int. Workshop Adv. Motion Control*, Mar. 2012, pp. 1–6.
[6] E. J. Rouse, L. M. Mooney, E. C. Martinez-Villalpando, and H. M. Herr, "Clutchable series-elastic actuator: Design of a robotic knee prosthesis for minimum energy consumption," in *Proc. IEEE 13th Int. Conf. Rehabil. Robot.*, Jun. 2013, pp. 1–6.
[7] W. M. dos Santos, G. A. P. Caurin, and A. A. G. Siqueira, "Design and control of an active knee orthosis driven by a rotary series elastic actuator," *Control Eng. Pract.*, vol. 58, pp. 307–318, Jan. 2017.
[8] D. Ragonesi, S. Agrawal, W. Sample, and T. Rahman, "Series elastic actuator control of a powered exoskeleton," in *Proc. Annu. Int. Conf. IEEE Eng. Med. Biol. Soc.*, Sep./Aug. 2011, pp. 3515–3518.
[9] A. Calanca, L. Capisani, and P. Fiorini, "Robust force control of series elastic actuators," *Actuators*, vol. 3, no. 3, pp. 182–204, 2014.
[10] D. W. Robinson, J. E. Pratt, D. J. Paluska, and G. A. Pratt, "Series elastic actuator development for a biomimetic walking robot," in *Proc. IEEE/ASME Int. Conf. Adv. Intell. Mechatronics*, Sep. 1999, pp. 561–568.
[11] G. Kwakkel, B. J. Kollen, and H. I. Krebs, "Effects of robot-assisted therapy on upper limb recovery after stroke: A systematic review," *Neurorehabilitation Neural Repair*, vol. 22, no. 2, pp. 111–121, Mar. 2008.
[12] A. G. L. Junior, R. M. de Andrade, and A. B. Filho, "Series elastic actuator: Design, analysis and comparison," *Recent Adv. Robot. Syst.*, vol. 1, pp. 203–234, Sep. 2016.
[13] A. G. Leal, Jr., *et al.*, "Polymer optical fiber for angle and torque measurements of a series elastic actuator's spring," *J. Lightw. Technol.*, vol. 36, no. 9, pp. 1698–1705, May 1, 2018.
[14] K. Peters, "Polymer optical fiber sensors—A review," *Smart Mater. Struct.*, vol. 20, no. 1, Dec. 2010, Art. no. 13002.
[15] K. Kalli *et al.*, "Electrically tunable Bragg gratings in single mode polymer optical fiber," *Opt. Lett.*, vol. 32, no. 3, pp. 214–216, 2007.
[16] G. Woyessa *et al.*, "Zeonex-PMMA microstructured polymer optical FBGs for simultaneous humidity and temperature sensing," *Opt. Lett.*, vol. 42, no. 6, pp. 1161–1164, 2017.
[17] Y. Zheng, K. Bremer, and B. Roth, "Investigating the strain, temperature and humidity sensitivity of a multimode graded-index perfluorinated polymer optical fiber with Bragg grating," *Sensors*, vol. 18, no. 5, pp. 1–10, May 2018.
[18] A. G. Leal, Jr., *et al.*, "Polymer optical fiber Bragg gratings in CYTOP fibers for angle measurement with dynamic compensation," *Polymers*, vol. 10, no. 6, p. 674, Jun. 2018.

[19] P. Savva, A. Theodosiou, M. Petrou, and K. Kall, "Concrete RH monitoring using embedded FBG sensors inscribed in multimode CYTOP fibre," in *Proc. 5th Workshop Specialty Opt. Fiber Their Appl.*, Oct. 2017, pp. 1–2.

[20] R. Ishikawa *et al.*, "Pressure dependence of fiber Bragg grating inscribed in perfluorinated polymer fiber," *IEEE Photon. Technol. Lett.*, vol. 29, no. 24, pp. 2167–2170, Dec. 15, 2017.

[21] X. Hu *et al.*, "Polarization effects in polymer FBGs: Study and use for transverse force sensing," *Opt. Express*, vol. 23, no. 4, pp. 4581–4590, 2015.

[22] C. Broadway *et al.*, "L-band CYTOP Bragg gratings for ultrasound sensing," in *Proc. Int. Soc. Opt. Photon.*, vol. 10681, pp. 1–8, May 2018.

[23] A. G. Leal, Jr., *et al.*, "Polymer optical fiber sensors in wearable devices: Toward novel instrumentation approaches for gait assistance devices," *IEEE Sensors J.*, vol. 18, no. 17, pp. 7085–7092, Sep. 2018.

[24] A. Cusano, A. Cutolo, and J. Albert, *Fiber Bragg Grating Sensors: Market Overview and New Perspectives*. Potomac, MD, USA: Bentham Science, 2009.

[25] G. D. Peng, Z. Xiong, and P. L. Chu, "Photosensitivity and gratings in dye-doped polymer optical fibers," *Opt. Fiber Technol.*, vol. 5, no. 2, pp. 242–251, Apr. 1999.

[26] A. Lacraz, M. Polis, A. Theodosiou, C. Koutsides, and K. Kalli, "Femtosecond laser inscribed Bragg gratings in low loss CYTOP polymer optical fiber," *IEEE Photon. Technol. Lett.*, vol. 27, no. 7, pp. 693–696, Apr. 1, 2015.

[27] A. Lacraz, A. Theodosiou, and K. Kalli, "Femtosecond laser inscribed Bragg grating arrays in long lengths of polymer optical fibres; A route to practical sensing with POF," *Electron. Lett.*, vol. 52, no. 19, pp. 1626–1627, Sep. 2016.

[28] Y. Luo, B. Yan, Q. Zhang, G.-D. Peng, J. Wen, and J. Zhang, "Fabrication of polymer optical fibre (POF) gratings," *Sensors*, vol. 17, no. 3, p. 511, Mar. 2017.

[29] A. Theodosiou, A. Lacraz, A. Stassis, C. Koutsides, M. Komodromos, and K. Kalli, "Plane-by-plane femtosecond laser inscription method for single-peak Bragg gratings in multimode CYTOP polymer optical fiber," *J. Lightw. Technol.*, vol. 35, no. 24, pp. 5404–5410, Dec. 15, 2017.

[30] A. Theodosiou *et al.*, "Modified fs-laser inscribed FBG array for rapid mode shape capture of free-free vibrating beams," *IEEE Photon. Technol. Lett.*, vol. 28, no. 14, pp. 1509–1512, Jul. 15, 2016.

[31] A. G. Leal, Jr., *et al.*, "Polymer optical fiber Bragg gratings in CYTOP fibers for angle measurement with dynamic compensation," *Polymers*, vol. 10, no. 6, p. 674, Jun. 2018.

[32] M. R. A. Sanchez *et al.*, "Fiber Bragg grating-based sensor for torque and angle measurement in a series elastic actuator's spring," *Appl. Opt.*, vol. 57, no. 27, pp. 7883–7890, 2018.

[33] J. Yi, X. Zhu, H. Zhang, L. Shen, and X. Qiao, "Spatial shape reconstruction using orthogonal fiber Bragg grating sensor array," *Mechatronics*, vol. 22, no. 6, pp. 679–687, Sep. 2012.

[34] C. Kirtley, *Clinical Gait Analysis: Theory and Practice*. Philadelphia, PA, USA: Elsevier, 2006.

[35] A. G. Leal, Jr., A. Theodosiou, C. Marques, M. J. Pontes, K. Kalli, and A. Frizera, "Thermal treatments and compensation techniques for the improved response of FBG sensors in POFs," *J. Lightw. Technol.*, vol. 36, no. 17, pp. 3611–3617, Sep. 1, 2018.

[36] A. G. Leal, Jr., *et al.*, "POF-IMU sensor system: A fusion between inertial measurement units and POF sensors for low-cost and highly reliable systems," *Opt. Fiber Technol.*, vol. 43, pp. 82–89, Jul. 2018.

[37] J. Z. Sasiadek and P. Hartana, "Sensor data fusion using Kalman filter," in *Proc. 3rd Int. Conf. Inf. Fusion*, vol. 2, Jul. 2000, pp. WED5/19-WED5/25.

[38] B. Feng, M. Fu, H. Ma, Y. Xia, and B. Wang, "Kalman filter with recursive covariance estimation—Sequentially estimating process noise covariance," *IEEE Trans. Ind. Electron.*, vol. 61, no. 11, pp. 6253–6263, Nov. 2014.

[39] F. Auger, M. Hilairet, J. M. Guerrero, E. Monmasson, T. Orlowska-Kowalska, and S. Katsura, "Industrial applications of the Kalman filter: A review," *IEEE Trans. Ind. Electron.*, vol. 60, no. 12, pp. 5458–5471, 2013.

Arnaldo G. Leal-Junior, photograph and biography not available at the time of publication.

Antreas Theodosiou, photograph and biography not available at the time of publication.

Rui Min, photograph and biography not available at the time of publication.

Jonathan Casas, photograph and biography not available at the time of publication.

Camilo R. Díaz, photograph and biography not available at the time of publication.

Wilian M. dos Santos, photograph and biography not available at the time of publication.

Maria José Pontes, photograph and biography not available at the time of publication.

Adriano A. G. Siqueira, photograph and biography not available at the time of publication.

Carlos Marques, photograph and biography not available at the time of publication.

Kyriacos Kalli, photograph and biography not available at the time of publication.

Anselmo Frizera, photograph and biography not available at the time of publication.